


ARTICLE

Insights revealed by the co-crystal structure of the *Saccharomyces cerevisiae* histidine phosphotransfer protein Ypd1 and the receiver domain of its downstream response regulator Ssk1

Katie M. Branscum¹ | Smita K. Menon¹ | Clay A. Foster^{1,2} | Ann H. West¹ 

¹Department of Chemistry and Biochemistry, University of Oklahoma, Norman, Oklahoma

²Department of Microbiology and Immunology, University of North Carolina, Chapel Hill, North Carolina

Correspondence

Ann H. West, Department of chemistry and biochemistry, University of Oklahoma, 101 Stephenson Parkway, Norman, OK 73019.
Email: awest@ou.edu

Funding information

Grayce B. Kerr Endowment; National Institute of General Medical Sciences, Grant/Award Number: P20GM103640; National Science Foundation, Grant/Award Number: MCB 1158319; Oklahoma Center for the Advancement of Science and Technology, Grant/Award Number: HR12-059

Abstract

Two-component signaling systems are the primary means by which bacteria, archaea, and certain plants and fungi react to their environments. The model yeast, *Saccharomyces cerevisiae*, uses the Sln1 signaling pathway to respond to hyperosmotic stress. This pathway contains a hybrid histidine kinase (Sln1) that autophosphorylates and transfers a phosphoryl group to its own receiver domain (R1). The phosphoryl group is then transferred to a histidine phosphotransfer protein (Ypd1) that finally passes it to the receiver domain (R2) of a downstream response regulator (Ssk1). Under normal conditions, Ssk1 is constitutively and preferentially phosphorylated in the phosphorelay. Upon detecting hyperosmotic stress, Ssk1 rapidly dephosphorylates and activates the high-osmolarity glycerol (HOG) pathway, initiating a response. Despite their distinct physiological roles, both Sln1 and Ssk1 bind to Ypd1 at a common docking site. Co-crystal structures of response regulators in complex with their phosphorelay partners are scarce, leaving many mechanistic and structural details uncharacterized for systems like the Sln1 pathway. In this work, we present the co-crystal structure of Ypd1 and a near wild-type variant of the receiver domain of Ssk1 (Ssk1-R2-W638A) at a resolution of 2.80 Å. Our structural analyses of Ypd1-receiver domain complexes, biochemical determination of binding affinities for Ssk1-R2 variants, in silico free energy estimates, and sequence comparisons reveal distinctive electrostatic properties of the Ypd1/Ssk1-R2-W638A complex that may provide insight into the regulation of the Sln1 pathway as a function of dynamic osmolyte concentration.

Abbreviations: ~F, fluoresceinated protein; ~P, phosphorylated protein; 5-IAF, 5-iodoacetamidofluorescein; HHK, hybrid histidine kinase; HK, histidine kinase; HPT, histidine phosphotransfer protein; IEX, ion exchange chromatography; MAD, multi-wavelength anomalous diffraction; MM/GBSA, Molecular Mechanics/Generalized Born Surface Area; RMSD, root mean square deviation; RR, response regulator; SEC, size exclusion chromatography.

This is an open access article under the terms of the Creative Commons Attribution-NonCommercial-NoDerivs License, which permits use and distribution in any medium, provided the original work is properly cited, the use is non-commercial and no modifications or adaptations are made.

© 2019 The Authors. *Protein Science* published by Wiley Periodicals, Inc. on behalf of The Protein Society.

KEYWORDS

two-component signaling, Ypd1, Ssk1, response regulator, histidine phosphotransfer protein, *Saccharomyces cerevisiae*, co-crystal, phosphotransfer

1 | INTRODUCTION

Two-component systems (TCSs) are the primary method of signal transduction in bacteria.^{1,2} In some eukaryotes, like plants and fungi, TCSs are expanded into multi-step phosphorelays involving hybrid sensor histidine kinases (HHKs), histidine phosphotransfer proteins (HPTs), and downstream response regulators (RRs).^{3–5} TCSs utilize the transmission of phosphoryl groups to internalize and respond to external stimuli. In the model yeast, *Saccharomyces cerevisiae*, the osmosensing pathway begins with the membrane-bound HHK, Sln1. Under normal conditions, Sln1 constitutively autophosphorylates on a histidine residue and transfers the phosphoryl group to an aspartic acid residue on an attached C-terminal receiver domain (R1). Next, the phosphoryl group is transferred to the cytosolic histidine phosphotransfer (HPT) protein, Ypd1. Under non-stress conditions, Ypd1 then transfers the phosphoryl group to a downstream RR, Ssk1.⁶ Under hyperosmotic stress, Sln1 autophosphorylation is inhibited, allowing unphosphorylated Ssk1 to accumulate and initiate glycerol production via the HOG pathway, ultimately restoring osmotic balance.^{6–8}

A key feature of the Sln1 pathway is the ability of Ypd1 to interact with multiple partners that share high structural similarity but fill distinct physiological roles. Ypd1 binds the upstream (Sln1-R1) and downstream (Ssk1-R2) receiver domains using a common hydrophobic docking site.⁹ How Ypd1 differentiates between the two RRs is of great interest, as selectivity is crucial for proper cellular regulation. Previous studies showed that Ypd1 exhibits a threefold preference for interaction with Ssk1-R2 over Sln1-R1 and forms an unusually stable signaling complex with the phosphorylated form of Ssk1-R2 (Ssk1-R2~P), extending its lifetime significantly *in vitro*.^{9,10} Ypd1 has no apparent effect on the lifetime of Sln1-R1~P, suggesting functionally distinct modes of interaction.¹⁰ These differences are further highlighted by the rate of dissociation and the directionality of phosphotransfer in the system. While reversible transfer between Ypd1 and Sln1-R1 is detectable, the dissociation rate of the Ypd1/Sln1-R1 complex is 30-fold faster than the rate of the reverse reaction, allowing 97% of Ypd1 to remain phosphorylated.¹¹ When Ypd1 encounters Ssk1-R2, the forward reaction is strongly favored, with no observable reverse transfer.¹¹ These data are consistent with the physiological roles of Sln1-R1

-serving a phosphorelay function and Ssk1-R2 acting as a phosphorylation-dependent regulator of the downstream HOG pathway.¹⁰ Ypd1 also fills a regulatory role within the pathway; its unusually stable signaling complex with Ssk1~P is believed to prevent accumulation of unphosphorylated, dimeric Ssk1 and the subsequent activation of the HOG pathway.^{8,10} Certain osmolytes, such as salt and glycerol, are known to affect the stability of the Ypd1/Ssk1-R2 complex.^{12,13} This effect, along with the extended half-life of its phosphorylated complex, suggests that the Ypd1/Ssk1-R2 interaction relies on an interesting signaling mechanism that may both respond to and be directly regulated by osmotic stress.

Characterizing the interactions between Ypd1 and its protein partners is a critical step in understanding the path of signal transduction within the system. However, the lack of structural information for the downstream RR (Ssk1) has made previous study of the interaction mechanisms in the Sln1 pathway challenging. Here, we present the 2.80 Å co-crystal structure of a eukaryotic HPT protein (Ypd1) in complex with a near wild-type variant of the receiver domain of its cognate downstream RR (Ssk1-R2-W638A). For the first time, we investigate differences in the binding interfaces between Ypd1 and its partners using the existing co-crystal complex of Ypd1/Sln1-R1 as a point of reference.¹⁴ Our comparison is further supported by sequence analysis, biochemical characterization, and computational studies to determine key residues involved in complex formation and phosphotransfer. We identify distinct electrostatic characteristics at the binding interface that strongly influence the Ypd1/Ssk1 interaction. The electrostatic forces are likely to be affected by the intracellular osmolyte levels, providing an explanation for how changes in the osmotic environment can alter the stability of the Ypd1/Ssk1 complex and ultimately influence the activation of the HOG pathway.

2 | RESULTS AND DISCUSSION

2.1 | Overall Structural Comparison of Ypd1/Ssk1-R2-W638A and Ypd1/Sln1-R1

The identification of a Trp-to-Ala substitution at position 638 in Ssk1-R2 (W638A) led to improved solubility and notable purification improvements over the intractable

wild-type protein, facilitating successful crystallization.¹⁵ Due to its location away from the functional surface of Ssk1-R2, the W638 residue is believed to have negligible effects on partner binding or phosphotransfer (Figure 1A). The Ypd1/Ssk1-R2-W638A co-crystal structure was determined using a selenomethionine derivative of Ssk1-R2-W638A. Crystallographic phase information was obtained using the multi-wavelength anomalous diffraction (MAD) technique.¹⁶ After several rounds of refinement using phenix.refine the R -factor was at 22.9% with an R_{free} of 27.9%.¹⁷ The final model was refined to a resolution of 2.80 Å (Table 1).

Our lab previously reported the co-crystal structure of Ypd1 bound with the receiver domain of its upstream partner (Sln1-R1) in an unphosphorylated state (PDB: 1OXB).¹⁴ This was used for comparison with the newly elucidated Ypd1/Ssk1-R2-W638A complex (Figure 1a).

To identify a structural basis for the unique features of the Ypd1/Ssk1-R2 interaction, we performed comprehensive analyses on the two receiver domain structures, including comparing docking orientations with regard to Ypd1 (Figure 1b), overall topologies (Figure 1c), intermolecular contacts (Table S1), and surface properties of both Sln1-R1 and Ssk1-R2-W638A (Figure 2). The Sln1 and Ssk1 receiver domains exhibited a highly similar ($\beta\alpha$)₅ topology. Structure-based alignment of the receiver domains showed an overall C α RMSD of \sim 0.89 Å, with larger deviations in the variable loop regions, such as the dynamic β 4- α 4 segment (up to 2.4 Å C α RMSD; Figure 1c, a corresponding sequence alignment is shown in Figure S1). Based on this alignment, two notable differences were observed at the α 3- β 4 loop with a 20-residue extension and a 50-residue extension at the C-terminal tail in Ssk1 (distal to the active site surface).

FIGURE 1 Structural comparison of Sln1-R1 and Ssk1-R2-W638A with Ypd1. (a) Ypd1 (green) adopts a four-helix bundle core; the active site histidine (H64) is depicted in stick format. The Ssk1-W638A receiver domain (blue) adopts the canonical RR ($\beta\alpha$)₅ fold; the active site aspartate residue (D554) is shown in stick format with the site of substitution (W638A) in cyan. (b) Sln1-R1 (magenta, PDB ID: 1OXB) and Ssk1-R2-W638A (blue, PDB ID: 5K BX) bind to Ypd1 (green) at the same hydrophobic docking site but adopt different rigid body positions. Complexes were structurally aligned using the C α atoms of the Ypd1 monomers. (c) Sln1-R1 (magenta) superpositioned with Ssk1-R2-W638A (blue). The sites of phosphorylation (Sln1-R1-D1144, Ssk1-R2-D554) are shown in stick format

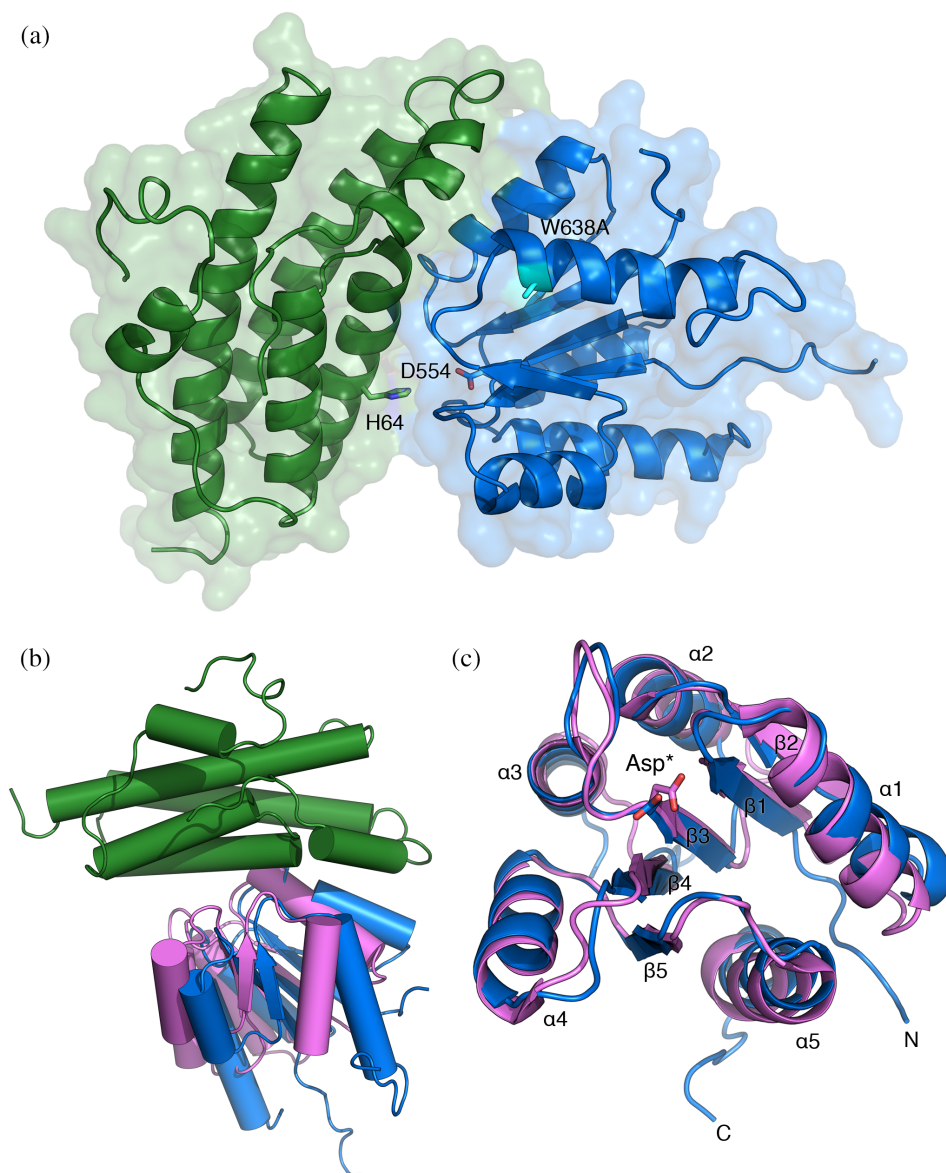


TABLE 1 X-ray data collection^b and refinement statistics

Data collection	Se-peak	Se-remote	Se-edge
Wavelength (Å)	0.9791	0.9116	0.9793
Temperature (°K)	100		
Resolution (Å)	33.27–2.80 (2.90–2.80)		
Reflections observed	12,051	12,033	12,010
Reflections observed after elliptical truncation	10,608	10,535	10,560
Redundancy	10.4	10.3	10.4
Completeness (%)	99.8 (99.5)	99.8 (100.00)	99.8 (99.7)
Completeness after elliptical truncation (%)	88.4 (44.6)	86.9 (35.05)	87.3 (41.2)
Mean I/σ (I)	43 (3.25)	40.6 (2.75)	42.7 (3.5)
R _{sym} ^a	0.055 (0.69)	0.062 (0.79)	0.058 (0.79)
Crystal parameters			
Space Group	P4 ₃ 2 ₁ 2		
Unit cell dimensions (Å)	71.69, 71.69, 176.38	71.73, 71.73, 176.47	71.74, 71.74, 176.51
Matthews' coefficient (Å ³ /Da)	2.51		
Solvent content (%)	51.00		
Refinement			
Resolution range (Å)	33.27–2.80		
Number of protein atoms	2377		
Average B-factors (Å ²)	42.19		
R-factor (%)	22.8		
R _{free} (%)	27.9		
RMSD bond lengths (Å)	0.001		
RMSD bond angles (°)	0.350		
Ramachandran plot (%)			
Most favored region	98.62		
Additionally allowed region	1.38		
Clash score	1.85		

^aR_{sym} = $\sum_h \sum_i |I_i(h) - \langle I(h) \rangle| / \sum_h \sum_i \langle I(h) \rangle$ where $I_i(h)$ is the i th measurement of reflection h and $\langle I(h) \rangle$ is the average value of the reflection intensity.

^bValues in parentheses are for highest-resolution shell.

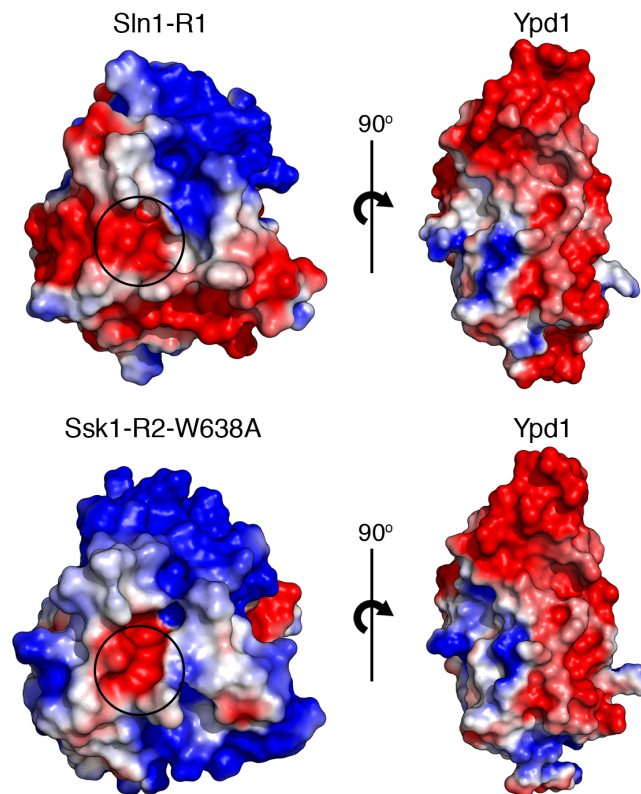


FIGURE 2 Electrostatic surface potential of Sln1-R1 and Ssk1-R2-W638A interfaces with Ypd1. Complexes were bisected and rotated to provide a frontal view of each binding interface. Top) Sln1-R1 (left) and Ypd1 (right). Bottom) Ssk1-R2-W638A (left) and Ypd1 (right). Red = electronegative, white = neutral, blue = electropositive. Phosphorylatable aspartate residue positions (Sln1-R1-D1144 and Ssk1-R2-W638A-D554; left) are circled in black

Electron density was not detected for these regions in the Ypd1/Ssk1-R2-W638A co-crystal structure, suggesting high flexibility. Additional deviations were found on the side of the receiver domains distal to the Ypd1 binding interface, including at the C-terminal ends of the $\alpha 1$ (up to 2.9 Å C α RMSD) and $\alpha 3$ (up to 2.2 Å C α RMSD) helices and at the $\alpha 2$ - $\beta 3$ loop (up to 1.9 Å C α RMSD). Although these features may affect the Ypd1/Ssk1-R2 interaction, their distance from the active site surface suggests that they are unlikely to play a major role in binding or catalysis.

2.2 | Interface characteristics of the Ypd1/Ssk1-R2-W638A and Ypd1/Sln1-R1 co-complexes

The Ypd1/Ssk1-R2-W638A co-crystal structure confirmed that a common hydrophobic binding surface is used by Ypd1 to interact with its cognate partners.⁹ However, a rigid-body shift of the receiver domain docking positions on Ypd1 (Figure 1b) suggested that their interfaces could be

distinct. The full functional implications of this rigid-body shift are unclear, though similar variations in rigid-body orientations have been observed in multiple HK/RR complexes.¹⁸ The shift results in noticeably increased distance between the conserved active site residues when compared to the Ypd1/Sln1-R1 structure. If the same orientation occurs during the wild-type Ypd1/Ssk1-R2 interaction, this may affect the reversibility of the phosphotransfer reaction between Ypd1 and the receiver domain.¹⁹ While the Ypd1/Ssk1-R2-W638A and Ypd1/Sln1-R1 complexes shared an approximately equal number of hydrophobic contacts between subunits (20 unique residues forming 15 intermolecular interactions vs. 24 unique residues forming 16 intermolecular interactions, respectively; determined with PDBsum), the Ypd1/Sln1-R1 structure exhibited several features typically associated with higher binding affinities.^{20–23} The Ypd1/Sln1-R1 interface contained nearly twice as many intermolecular hydrogen bonds, and the overall binding interface of Sln1-R1 was ~24% larger than that of Ssk1-R2-W638A (based on the largest interfaces detected with PDBEPIA).²⁴ An overview of the various intermolecular interactions observed at each of the Ypd1/Ssk1-R2-W638A and Sln1-R1 interfaces can be found in Table S1 (generated with PDBsum).²³ These features offer little explanation for the interaction and phosphotransfer preference for wild-type Ssk1-R2 exhibited by Ypd1 in previous work.^{9,11} Due to the constitutively phosphorylated nature of Ssk1-R2 under nonstress conditions, we cannot rule out the possibility of significant phosphorylation-dependent changes at the Ypd1/Ssk1-R2 interface. Structural studies incorporating a phosphoryl analog will likely provide more insight, though efforts utilizing BeF_3^- have thus far been unsuccessful.

Further analyses of the interfaces revealed distinct electrostatic profiles for the receiver domain binding surfaces. Electrostatic potential maps (Figure 2) suggested that Ssk1-R2-W638A possesses a binding interface that is highly complementary to the electronegative surface of Ypd1. Charge complementarity can affect association rates through a phenomenon known as electrostatic steering, often leading to higher apparent binding affinities.^{12,22,25–28} This is likely related to previous findings that described an osmolyte-dependence on the affinity of wild-type Ssk1 for Ypd1, while interactions between wild-type Sln1 and Ypd1 were minimally affected.^{12,13}

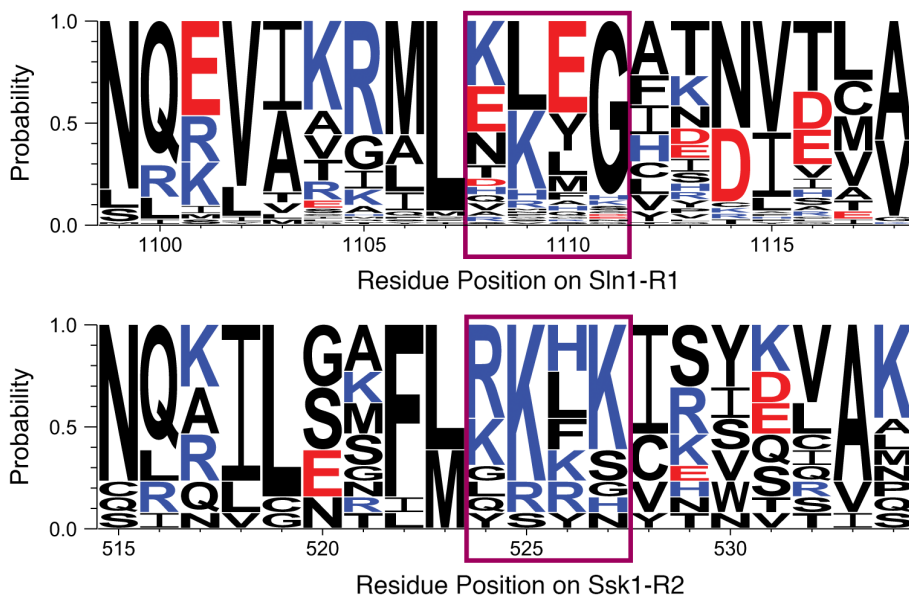
To analyze the electrostatic nature of specific regions in direct contact within each complex, we searched both binding surfaces for explicit intermolecular salt bridges. At the Ypd1/Sln1-R1 interface, two theoretical salt bridges were seen in the active site: H64 in Ypd1 can potentially form a salt bridge with both D1144 and D1095 in Sln1-R1. These interactions are unlikely to occur during prephosphotransfer complex formation between

phosphorylated Sln1-R1 and Ypd1, as D1144 is the phosphorylatable aspartate residue and D1095 is responsible for binding to a Mg^{2+} cation.²⁹ These interactions were not detected when we analyzed a separate, activated (BeF_3^- -bound) Ypd1/Sln1-R1 structure (PDB: 2R25).²⁹ In contrast, the Ypd1/Ssk1-R2-W638A structure contained an extra salt bridge cluster at the edge of the binding interface (Figure 3a). One salt bridge was located within the active site: H64 of Ypd1 can form a potential salt bridge with D511 of Ssk1-R2-W638A. An additional salt bridge cluster was observed near the highly negative loop residues D21-D22-D23-D24 between the αA and αB helices of Ypd1 and R524 on the α1 helix of Ssk1-R2-W638A (Figure 3b). The proximity of K525 on Ssk1-R2-W638A suggests that it is likely able to form a salt bridge as well. The addition of ionic tethers at a protein-protein interface can greatly affect the apparent binding behavior and overall hydrogen-bonding network of the complex.²² A pair of positively charged residues was also observed on the α1 helix of Sln1-R1 (K1104 and R1105) in the Ypd1/Sln1-R1 structure; however, the rotated orientations and increased distance between these charged residues and the negatively charged loop on Ypd1 within the complex suggested that they are less ideal for participating in intermolecular ionic interaction(s). The same altered orientations were observed in the activated Ypd1/Sln1-R1 structure. However, considering the flexible loop-like nature of the corresponding region on Ypd1, it seems reasonable that R1105 could participate in a salt bridge interaction with Ypd1. Two additional electropositive residues (H526 and K527) were seen directly C-terminal to the putative salt-bridge residues R524 and K525 on Ssk1-R2-W638A. No such residues were found on Sln1-R1; in fact, several negatively charged glutamate residues are located near the site. While the possibility of a more transient intermolecular salt bridge forming between Sln1-R1 and Ypd1 at the R1105 position should not be ruled out, these findings suggested a significantly elevated concentration of electropositive potential on the C-terminus of α1 in Ssk1-R2.

2.3 | Sequence analysis and conservation of electrostatic properties

The distribution of charged residues in the α1 helix is illustrated in Figure 4. A structure-based sequence alignment of Ssk1-R2, Sln1-R1, and various representative RRs was used to compare the electrostatic nature of the region among other well-characterized proteins. Most RRs exhibited a concentration of electropositive residues near the acidic Mg^{2+} -binding residues (Figure 4, green and pink bars). In Ssk1-R2, this increased density of electropositivity was shifted and extended toward the C-terminus (Figure 4, blue

FIGURE 5 Residue distributions for upstream (top; analogous to Sln1-R1) and downstream (bottom; analogous to Ssk1-R2) receiver domains near the salt bridge cluster of the Ypd1/Ssk1-R2 interface. Eukaryotic RR sequences involved in osmotic stress response were aligned and categorized into “upstream” (containing HHK domains) and “downstream” (receiver domains lacking a kinase domain) groups. Rectangles indicate positions R524-K525-H526-K527 in Ssk1-R2 and the corresponding region in Sln1-R1. Residues are colored by charge (blue, electropositive, red, electronegative, black, neutral)



osmosensing from the UniProt database.³² Proteins were divided into two groups corresponding to upstream and downstream elements of a pathway, respectively: receiver domains located on a HHK, and receiver domains lacking a kinase domain. These groups were considered analogous to the relationship between Sln1-R1 and Ssk1-R2. Both groups were aligned, and residue distributions were visualized for the regions corresponding to positions 515–534 on Ssk1-R2 (Figure 5). The graphics revealed a distinguishable pattern between the two RR groups. Receiver domains analogous to Ssk1-R2 exhibited enrichment for electropositive residues at the C-terminal end of the α 1 helix, while the HHK receiver domains exhibited considerably less conservation and more negatively charged amino acids. The individual sequence groups were directly compared to test for differences in amino acid distributions based on physicochemical properties.³³ Positively charged and aromatic residues were significantly enriched ($p < .001$) within the Ssk1-R2 group (13 sequences), while negatively charged residues were significantly depleted ($p < .001$) when compared to the Sln1-R1/HHK group (75 sequences). While our analysis was limited by the extent and accuracy of GO term annotations within the database, the striking prevalence of electropositive residues in the group analogous to Ssk1-R2 implied a potential functional relevance for these residues.

2.4 | Investigation of the contribution of specific amino acids to Ypd1/Ssk1-R2 binding

To further examine the electrostatic complementarity observed in the Ypd1/Ssk1-R2-W638A complex, we

analyzed the roles of specific amino acids on Ssk1-R2 with respect to binding affinity. We hypothesized that certain electrostatic interactions (primarily the salt bridges formed between Ssk1-R2-R524/K525 and Ypd1-D23/D24) significantly contribute to the affinity between Ypd1 and Ssk1-R2. We first calculated the per-residue contributions to binding energy for the complex using the Molecular Mechanics/Generalized Born Surface Area technique (MM/GBSA) (Table 2). These estimates highlighted the significant roles of Ssk1-R2 residues I518, R524, and K525 in Ypd1 binding; all three residues provided favorable contributions of approximately 2 kcal/mol or more. Previous work suggested that I518 is located within the hydrophobic binding surface, while the considerable contributions from R524 and K525 supported the hypothesis that electrostatic forces play a major role in complex formation.^{8,34}

To confirm the estimates, an *in vitro* fluorescence-binding assay was used to measure relative binding affinities between Ypd1 and Ssk1-R2 variants that we created to disrupt these interactions.³⁵ A threonine residue (T12) near the binding surface of Ypd1 was substituted with cysteine (T12C) and labeled with 5-iodoacetamidofluorescein (5-IAF). Titrations of Ssk1-R2 variants affected the fluorescence of 5-IAF-labeled Ypd1-T12C in a concentration-dependent manner (Figure S3). Binding data were corrected for dilution and fitted using an expanded quadratic equation to obtain apparent equilibrium dissociation constants. Binding curves for Ssk1-R2-R524A and K525A (Figure S3, green and blue) exhibited highly diminished signal changes relative to wild-type, up to maximum attainable concentrations (μ M range; data not shown). Curves for Ssk1-R2-I518S (Figure S3, red) resembled the buffer control (also extended to a maximum attainable

TABLE 2 Observed binding affinities between Ypd1 and Ssk1-R2 Variants

Ssk1-R2 variant	Obs. K_d with Ypd1-T12C~F \pm SD (nM)	$\Delta\Delta G_{\text{binding}}$ (kcal/mol)	Contribution \pm SD (kcal/mol, GB ^{NECK2})
WT	23.7 \pm 2.0	–	–
I518S	Not determinable	–	–4.1 \pm 0.6
R524A	918.0 \pm 460.4	2.2	–1.9 \pm 1.6
K525A	640.4 \pm 178.8	1.9	–3.2 \pm 1.4
W638A	219.1 \pm 29.4	1.3	–0.01 \pm 0.02

Note. Multiple replicates were run for each variant ($n = 3-5$).

concentration in the μM range). We inferred from their flattened binding curves that all three substitutions negatively affected binding to Ypd1. Apparent K_d values for both salt bridge substitutions were considerably higher than wild-type ($\sim 28-39$ -fold increases). These results highlight the significant role played by electrostatic interactions in the Ypd1/Ssk1-R2 complex. This is consistent with previous findings that the introduction of complementary charged residues near equivalent positions in the Ypd1/Sln1-R1 complex can affect both binding affinity and sensitivity to salt, as well as the negative relationship observed between Ypd1/Ssk1-R2~P stability and osmolyte levels.^{12,13}

To compare the predicted per-residue contributions to binding free energy with the experimentally determined affinities of the Ssk1-R2 variants, observed dissociation constants were converted to $\Delta\Delta G_{\text{binding}}$ estimates (Equation 1, Table 2). The predicted free energy values correlated well with the observed phenotypes; deleterious substitutions at highly favorable binding positions led to large positive increases in the free energies of binding. Ablating the salt bridge interactions substantially reduced the affinity between Ssk1 and Ypd1, although binding was still detectable for both variants (Table 2, Figure S3). Interestingly, the $\Delta\Delta G_{\text{binding}}$ for the W638A substitution revealed a ninefold decrease in the observed binding affinity between Ypd1 and Ssk1-R2-W638A compared to wild-type (Table 2), deviating from the in silico predictions. The direction of the fluorescence change was also inverted in experiments involving Ssk1-R2-W638A when compared to the other Ssk1-R2 variants (R2-W638A curves were converted for visualization). The possibility exists that the W638A substitution has a destabilizing effect on the structure of Ssk1-R2. Due to its location on the $\alpha 4$ - $\beta 5$ - $\alpha 5$ surface and its proximity to the aromatic switch residue (Y629), the indole side chain of W638 could likely interact in some capacity with functionally important residues involved in phosphorylation-dependent conformational transitions. Changes to these interactions may affect partner binding

and/or phosphotransfer. However, given the inverted fluorescence signal and the low predicted free energy contributions at this position, we hypothesize that during the binding assay, a π -stacking interaction occurred between the indole ring of wild-type Ssk1-R2-W638 and the 5-IAF fluorophore attached to Ypd1-T12C.¹⁵ This may have increased the observed binding affinity for Ypd1 in all Ssk1-R2 variants. The signal inversion was likely due to the loss of the indole ring in the W638A substitution. Removal of the nearby H637 imidazole ring produced a similar decrease in affinity (West lab, H637A, data not shown). The observed dissociation constants with Ypd1-T12C~F were calculated to be in the nM range for all Ssk1-R2 variants, 2- to 10-fold lower than the estimated dissociation constant for the Ypd1/Sln1-R1 interaction.³⁵ However, interaction between W638 (and/or H637) and the 5-IAF fluorophore likely increased the apparent affinity between Ssk1-R2 and labeled Ypd1, and a closer estimate of an absolute K_d may be higher. This would be consistent with previously reported binding affinities between Ssk1-R2 and Ypd1.¹¹⁻¹³ This highlights the importance of considering the observed kinetic data of the Ssk1-R2 variants in relative terms ($\Delta\Delta G_{\text{binding}}$), rather than as absolute representations of equilibrium dissociation constants.

Finally, we examined the Ssk1 variants using an in vitro phosphotransfer assay (see Supporting Information S1) to test for phospho-accepting ability, phospho-stability, and phosphotransfer preference in relation to wild-type Ssk1-R2. Ssk1-R2-W638A was found to possess a phosphorylated lifetime and phospho-accepting ability that was comparable to wild-type. Moderate reverse phosphotransfer (Ssk1-R2 to Ypd1) was detected when using the Ssk1-R2-W638A variant, unlike the exclusively unidirectional reaction seen in the wild-type complex. We speculate that these observations may be related to changes in the geometry of the conserved active site residues in the wild-type and variant Ypd1/Ssk1-R2 complexes relative to the Ypd1/Sln1-R1 complex, although additional in silico studies and/or a BeF_3^- bound structure of Ypd1/Ssk1-R2 would provide a more definitive analysis. The loss of the indole ring at position 638 in the Ssk1-R2-W638A variant may also affect the aromatic Y629 switch residue involved in phosphorylation-dependent conformational transitions, potentially affecting the reversibility of the phosphotransfer reaction. While the I518S variant was largely unable to receive the phosphoryl group from Ypd1 (Figure S4), the R524A and K525A variants both exhibited near wild-type activity (Figure S5), suggesting that the substitutions did not grossly affect the topology of the protein. These findings indicate that removing a single residue from the electropositive cluster (R524-K525-H526-K527) on Ssk1-R2 is not sufficient to completely disrupt the pathway under these

conditions, despite causing a significant drop in apparent binding affinity. It is reasonable to assume that more complete ablation of the electrostatic network near Ssk1-R2-R524 would have a proportionally negative effect on enzymatic function; however, multiple substitutions within the receiver domain have proven intractable.

3 | DISCUSSION

We have presented and characterized the co-crystal structure of the eukaryotic HPt protein, Ypd1, in complex with its downstream response regulator, Ssk1-R2-W638A. Supporting biochemical studies revealed that Ssk1-R2-W638A possesses the following properties: wild-type levels of phosphoaccepting ability; a phosphorylated half-life indistinguishable from wild-type Ssk1-R2; and only a moderate difference in binding affinity for Ypd1, indicating that insights provided by the co-crystal structure have physiological relevance. Our analysis also revealed that Ssk1-R2 shares distinct and extensive overall charge complementarity with Ypd1 along the interaction surface. Sequence comparisons suggested that this complementarity may be conserved on the $\alpha 1$ helix in other response regulators involved in osmotic stress response, implying a deeper functional significance. Two intermolecular salt bridges involving residues R524 and K525 on Ssk1-R2 were identified that when neutralized, greatly diminished the binding affinity between Ypd1 and Ssk1-R2, implicating the importance of these residues in the interaction between Ypd1 and its downstream cognate partner. The role of electrostatic forces in the Ypd1/Ssk1-R2 interaction offers a means for influencing the Sln1 pathway through dynamic osmolyte concentrations, which can affect the stability of the Ypd1/Ssk1-R2 complex.^{12,13} However, disruption of the complex alone is unlikely to account for the rapid increase in unphosphorylated Ssk1-R2 in response to stress, based on the estimated half-life of Ssk1-R2~P (20 min, see Supporting Information S1) and the apparent activation time of the Sln1 pathway upon stimulation (2 min).^{8,12} Other partially redundant systems or contributing elements such as phosphatases may also be involved in the fungal osmotic stress response. The function of this region is also unclear in the Ypd1/Sln1-R1 complex, specifically involving the previously mentioned R1105 residue that was observed in the receiver domain, which may also participate in an intermolecular ionic interaction with Ypd1. Additional work is needed to more fully characterize the role of this area in both the Ypd1/Ssk1-R2 and Ypd1/Sln1-R1 interactions. The newly determined co-crystal structure of Ypd1/Ssk1-R2-W638A provides a valuable starting point for this and other future studies to better understand the yeast osmoregulatory system.

4 | MATERIALS AND METHODS

4.1 | Site-directed mutagenesis

Ssk1 variants were constructed from the Ssk1-R2 plasmid using the QuikChange (Agilent, Santa Clara, California) or Q5 (New England BioLabs, Ipswich, Massachusetts) methods.³⁶ Ypd1-T12C was constructed from the Ypd1 wild-type expression plasmid.³⁷ DNA was sequenced at the DNA Sequencing facility at Oklahoma Medical Research Foundation (OMRF, Oklahoma City, Oklahoma).

4.2 | Protein purification

Ypd1 from *S. cerevisiae* (and Ypd1-T12C) was purified from *Escherichia coli* DH5 α cells as a tag-less, full-length protein by ammonium sulfate precipitation, IEX, and SEC.^{37,38} Ssk1-R2 was purified using the IMPACT system (NEB) followed by SEC.³⁶ For the fluorescence assay, Ssk1-R2 variants were flash-frozen and stored in buffer (20 mM Tris pH 8.0, 500 mM NaCl, 10% glycerol) passed through Chelex (Bio-Rad, Hercules, California) resin. Variants were purified in a similar manner as wild-type. Selenomethionine-incorporated Ssk1-R2-W638A was produced by *E. coli* grown in M9 minimal media supplemented with selenomethionine and other amino acids.³⁹ Subsequent purification steps were identical to wild-type Ssk1-R2.

4.3 | Crystallization and data collection

Ssk1-R2-W638A and Ypd1 were mixed together in an equimolar ratio and co-concentrated to ~15 mg/ml. Crystals were obtained in 0.2 M Li₂SO₄, 0.1 M CAPS/NaOH pH 10.5, 1.2 M NaH₂PO₄/0.8 M K₂HPO₄. Hanging drop optimization screens (24-well) were set up around these conditions using proteins co-concentrated in 50 mM Tris pH 8.0, 100 mM NaCl and 1% glycerol. Resulting crystals diffracted to 3.0 Å at 100 K at the Macromolecular Crystallography Laboratory at the University of Oklahoma (Rigaku 007HF Micromax generator with CuK α line and a Dectris Pilatus 200 K detector). To collect independent phasing information, a selenomethionine-derivative of Ssk1-R2-W638A was created and co-crystallized with Ypd1. Crystals were cryoprotected using 1.2 M NaH₂PO₄, 0.8 M K₂HPO₄, 0.2 M Li₂SO₄, 0.1 M CAPS pH 10.5, and 9% glycerol. A MAD data set was collected at the Stanford Synchrotron Radiation Lightsource (SSRL) at 100 K on beam line 11-1.

4.4 | Structure determination, refinement and analysis

Data were indexed and scaled using HKL-2000 for all three wavelengths.⁴⁰ To account for severe anisotropy observed in all datasets, an elliptical correction was applied to the merged dataset using ctruncate from the CCP4 software suite.^{41,42} Data were submitted to the UCLA-DOE diffraction anisotropy server, which suggested diffraction limits of 3.0, 3.0, and 2.6 along the a^* , b^* , and c^* axes.⁴³ The structure of the Ssk1-R2-W638A RR receiver domain in complex with Ypd1 was determined using phasing information obtained from AutoSol in PHENIX-1.9-1692.¹⁶ Nontruncated data were used to compute the phases. For refinement with phenix.refine, elliptically truncated data from the peak wavelength were merged with the R_{free} flags generated by AutoSol and used as the input for all further refinement runs.^{16,17} Standard truncation results in 100% completeness at a resolution of 3.1 Å. TLS parameters were applied for terminal model refinement runs, with Chain A as 1 group and chain B split into four groups (based on chain breaks).¹⁷ Structural models were generated and analyzed using PyMOL and Chimera.^{44,45} Electrostatic potentials were calculated using the PDB2PQR/APBS server (CHARMM27 force field, protonation states assigned using PROPKA, 100 mM KCl, pH 7.0) and visualized using PyMOL.^{45–48}

4.5 | Sequence analysis

PROMALS3D was used to generate a structure-based sequence alignment of representative RR proteins for initial comparison.⁴⁹ A comprehensive RR sequence alignment was generated with MAFFT using RR receiver domain sequences obtained from Pfam.^{31,50,51} Gaps were removed using Ssk1-R2 as a reference. Pseudo-receiver domains were manually excluded. A sequence redundancy threshold of 90% was applied to reduce phylogenetic bias. For the HPT alignment, full-length sequences for HPT-containing proteins were obtained from Pfam and aligned to the pre-existing HPT HMM using hmalign.^{50,52} This was truncated to retain only canonical HPT domains and residues immediately N-terminal, in order to include the region corresponding to the negatively charged αA - αB “elbow” of Ypd1. The clipped sequences were realigned using MAFFT and a sequence redundancy threshold of 90% was again used. Eukaryotic RR receiver domain sequences annotated with GO terms related to “osmosensing” and “osmotic stress” (see Table S2) were obtained from the UniProt database.³² RRs were categorized into “upstream” (attached to HHKs) and “downstream” (all other receiver domains) groups analogous to

Sln1-R1 and Ssk1-R2, respectively. Sequences were aligned with MAFFT. Gaps were removed using Sln1-R1 and Ssk1-R2 as references, and a 90% sequence redundancy threshold was applied once again. WebLogos were generated to visualize amino acid frequencies within each group.³⁰ Analysis of amino acid distributions was performed with Composition Profiler using a Bonferroni adjusted α level of 1.25×10^{-3} per test to control for false positives.³³

4.6 | Fluorescence-binding assay

A fluoresceinated Ypd1-T12C variant (Ypd1-T12C~F) was created and used to test binding affinities with Ssk1-R2 variants as previously described.³⁵ Briefly, proteins were thawed and equilibrated (23°C) before each use. Ypd1-T12C~F was added to a quartz cuvette containing 50 mM Tris-HCl pH 8.0, 10 mM MgCl₂, and 1 mM DTT in a total volume of 2.5 ml. All buffers were passed through a 10 ml Chelex (Bio-Rad) column before use. Ssk1-R2 variants were titrated into the cuvette to a final volume of 2.7 ml. The reaction was subjected to gentle mixing and equilibration for 20 s after each injection. Fluorescence was then recorded to generate an equilibrium-binding curve. Ssk1-R2 concentrations were optimized for each assay, and Ypd1-T12C~F concentration was set to 6, 15, or 30 nM, depending on the expected K_d . Assays were designed to bracket the expected observed K_d with titrations. Excitation and emission wavelengths were set to 488 and 515 nm, respectively (Fluoromax-4 Spectrofluorometer from Horiba Scientific [Piscataway, New Jersey] slit widths set to 5 nm, 23 C). Fluorescence measurements were corrected for dilution prior to analysis. Curves were converted to fractional fluorescence (F/F_0) and shifted to begin at the origin for comparison purposes ($(F/F_0 - 1)$ for Ssk1-R2-W638A; $(1 - F/F_0)$ for all other Ssk1-R2 variants). GraphPad Prism (v.8) was used to fit the data using an expanded quadratic equation to account for fluorescence from both bound and unbound states of Ypd1.³⁵ $\Delta\Delta G_{\text{binding}}$ values for each variant were determined using the relationship described by Equation 1.

$\Delta\Delta G_{\text{binding}}$ between Ssk1-R2 variants with Ypd1-T12C~F.

$$\Delta\Delta G_{\text{binding}} = \frac{RT \cdot \ln\left(\frac{\kappa}{K_{d,\text{wild type}}}\right)}{4184 \frac{\text{J}}{\text{kcal}}} \quad (1)$$

R , gas constant (8.314462 J K⁻¹ mol⁻¹) and T , temperature (296 K).

4.7 | Molecular dynamics simulations and per-residue contributions to free energy of binding

A tryptophan residue was first modeled back at position 638 in Ssk1-R2-W638A. System preparation was done in VMD.⁵³ Regions of ambiguous electron density on Ssk1-R2 were excluded. The complex was solvated using the TIP3P model with 10 Å padding, then neutralized and ionized to a final concentration of 0.1 M KCl. Simulations were performed using NAMD (v.2.9) with the CHARMM36 force field release.^{54,55} Four independent replicates were run using random initial velocities. Initial energy minimization and equilibration was performed under a constant pressure using gradually decreasing atomic restraints over approximately 10 ns. Replicates were then run unrestrained for another 140 ns using an integration time step of 2 fs. The last 100 ns of each production run were retained for further analysis to ensure adequate equilibration.

Free energy calculations were done with the *MMPBSA.py* script provided in AmberTools16.⁵⁶ Salt concentration was set to 100 mM. Binding free energies were estimated with the Molecular Mechanics/Generalized Born Surface Area technique (MM/GBSA) using a modified Generalized Born model (GB^{NECK2}; *igb* = 8).⁵⁷ Additional GB models were explored with similar results.^{58–60} Approximately 375 frames per replicate at even intervals of 80 ps were included for the final calculations. Different intervals and effective trajectory lengths were tested with similar outcomes. Residue contributions to binding free energy were determined with the *decomp* module.⁶¹ Entropic contributions were ignored for computational efficiency.

PROTEIN STRUCTURE ACCESSION NUMBER

The atomic coordinates and structure factors for the Ypd1/Ssk1-R2-W638A complex have been deposited in RCSB PDB with PDB ID: 5KBX.

ACKNOWLEDGMENTS

We thank F. Janiak-Spens and E. Kennedy for their helpful comments during preparation of the manuscript. This work was supported by grants to AHW from the National Science Foundation (MCB 1158319), the Oklahoma Center for the Advancement of Science and Technology (HR12-059) and the Grayce B. Kerr endowment funds. Computing resources were provided by the OU Supercomputing Center for Education and Research (OSCAR). We gratefully acknowledge the use of the Macromolecular Crystallography Laboratory and the Protein Production

Core facilities at the University of Oklahoma, both of which are supported by an Institutional Development Award (IDeA) from the National Institute of General Medical Sciences of the National Institutes of Health under grant number P20GM103640. We are also grateful to the Stanford Synchrotron Radiation Light-source (SSRL) for access to their beam lines for crystallographic data collection. The SSRL Structural Molecular Biology Program is supported by the DOE Office of Biological and Environmental Research, and by the National Institutes of Health, National Institute of General Medical Sciences. The contents of this publication are solely the responsibility of the authors and do not necessarily represent the official views of NIGMS or NIH.

CONFLICT OF INTEREST

The authors have no conflict of interest to declare.

REFERENCES

1. Stock AM, Robinson VL, Goudreau PN. Two-component signal transduction. *Annu Rev Biochem.* 2000;69:183–215.
2. Bourret RB, Silversmith RE. Two-component signal transduction. *Curr Opin Microbiol.* 2010;13:113–115.
3. Saito H. Histidine phosphorylation and two-component signaling in eukaryotic cells. *Chem Rev.* 2001;101:2497–2509.
4. Fassler JS, West AH. Histidine phosphotransfer proteins in fungal two-component signal transduction pathways. *Eukaryotic Cell.* 2013;12:1052–1060.
5. Schaller GE, Shiu SH, Armitage JP. Two-component systems and their co-option for eukaryotic signal transduction. *Curr Biol.* 2011;21:R320–R330.
6. Posas F, Wurgler-Murphy SM, Maeda T, Witten EA, Thai TC, Saito H. Yeast HOG1 MAP kinase cascade is regulated by a multistep phosphorelay mechanism in the SLN1-YPD1-SSK1 “two-component” osmosensor. *Cell.* 1996;86:865–875.
7. Saito H, Posas F. Response to hyperosmotic stress. *Genetics.* 2012;192:289–318.
8. Horie T, Tatebayashi K, Yamada R, Saito H. Phosphorylated Ssk1 prevents unphosphorylated Ssk1 from activating the Ssk2 MAP kinase kinase kinase in the yeast HOG osmoregulatory pathway. *Mol Cell Biol.* 2008;28:5172–5183.
9. Porter SW, West AH. A common docking site for response regulators on the yeast phosphorelay protein YPD1. *Biochim Biophys Acta.* 2005;1748:138–145.
10. Janiak-Spens F, Sparling DP, West AH. Novel role for an HPT domain in stabilizing the phosphorylated state of a response regulator domain. *J Bacteriol.* 2000;182:6673–6678.
11. Janiak-Spens F, Cook PF, West AH. Kinetic analysis of YPD1-dependent phosphotransfer reactions in the yeast osmoregulatory phosphorelay system. *Biochemistry.* 2005;44:377–386.
12. Stojanovski K, Ferrar T, Benisty H, et al. Interaction dynamics determine signaling and output pathway responses. *Cell Rep.* 2017;19:136–149.
13. Kaserer AO, Andi B, Cook PF, West AH. Effects of osmolytes on the SLN1-YPD1-SSK1 phosphorelay system from *Saccharomyces cerevisiae*. *Biochemistry.* 2009;48:8044–8050.

14. Xu Q, Porter SW, West AH. The yeast YPD1/SLN1 complex: Insights into molecular recognition in two-component systems. *Structure*. 2003;11:1569–1581.
15. Branscum K. Structural and mutagenesis studies of the yeast phosphorelay signaling proteins Ypd1 and Ssk1 [Dissertation]. Norman: University of Oklahoma; 2015.
16. Adams PD, Afonine PV, Bunkoczi G, et al. PHENIX: A comprehensive python-based system for macromolecular structure solution. *Acta Cryst D*. 2010;66:213–221.
17. Afonine PV, Grosse-Kunstleve RW, Echols N, et al. Towards automated crystallographic structure refinement with phenix.refine. *Acta Cryst D*. 2012;68:352–367.
18. Buschiazzo A, Trajtenberg F. Two-component sensing and regulation: How do histidine kinases talk with response regulators at the molecular level? *Annu Rev Microbiol*. 2019;73:507–528.
19. Trajtenberg F, Imelio JA, Machado MR, et al. Regulation of signaling directionality revealed by 3D snapshots of a kinase:regulator complex in action. *eLife*. 2016;5:e21422.
20. Chen J, Sawyer N, Regan L. Protein–protein interactions: General trends in the relationship between binding affinity and interfacial buried surface area. *Protein Sci*. 2013;22:510–515.
21. Jones S, Thornton JM. Principles of protein-protein interactions. *Proc Natl Acad Sci USA*. 1996;93:13–20.
22. Sheinerman FB, Norel R, Honig B. Electrostatic aspects of protein–protein interactions. *Curr Opin Struct Biol*. 2000;10:153–159.
23. Laskowski RA, Jabłońska J, Pravda L, Vařeková RS, Thornton JM. PDBsum: Structural summaries of PDB entries. *Protein Sci*. 2018;27:129–134.
24. Krissinel E, Henrick K. Protein interfaces, surfaces and assemblies' service PISA at the European Bioinformatics Institute (http://www.ebi.ac.uk/pdbe/prot_int/pistart.html); Inference of macromolecular assemblies from crystalline state. *J Mol Biol*. 2007;372:774–797.
25. Kiel C, Selzer T, Shaul Y, Schreiber G, Herrmann C. Electrostatically optimized Ras-binding Ral guanine dissociation stimulator mutants increase the rate of association by stabilizing the encounter complex. *Proc Natl Acad Sci USA*. 2004;101:9223.
26. Linnemann T, Kiel C, Herter P, Herrmann C. The activation of RalGDS can be achieved independently of its Ras binding domain: Implications of an activation mechanism in Ras effector specificity signal distribution. *J Biol Chem*. 2002;277:7831–7837.
27. Sydor JR, Engelhard M, Wittinghofer A, Goody RS, Herrmann C. Transient kinetic studies on the interaction of Ras and the Ras-binding domain of c-Raf-1 reveal rapid equilibration of the complex. *Biochemistry*. 1998;37:14292–14299.
28. Zhang Z, Witham S, Alexov E. On the role of electrostatics in protein–protein interactions. *Phys Biol*. 2011;8:035001.
29. Zhao X, Copeland DM, Soares AS, West AH. Crystal structure of a complex between the phosphorelay protein YPD1 and the response regulator domain of SLN1 bound to a phosphoryl analog. *J Mol Biol*. 2008;375:1141–1151.
30. Crooks GE, Hon G, Chandonia J-M, Brenner SE. WebLogo: A sequence logo generator. *Genome Res*. 2004;14:1188–1190.
31. Chen C, Natale DA, Finn RD, et al. Representative proteomes: A stable, scalable and unbiased proteome set for sequence analysis and functional annotation. *PLOS ONE*. 2011;6:e18910.
32. UniProt Consortium T. UniProt: The universal protein knowledgebase. *Nucleic Acids Res*. 2018;46:2699–2699.
33. Vacic V, Uversky VN, Dunker AK, Lonardi S. Composition Profiler: A tool for discovery and visualization of amino acid composition differences. *BMC Bioinform*. 2007;8:211.
34. Li X, Keskin O, Ma B, Nussinov R, Liang J. Protein-protein interactions: Hot spots and structurally conserved residues often locate in complemented pockets that pre-organized in the unbound states: implications for docking. *J Mol Biol*. 2004;344:781–795.
35. Kennedy EN, Hebdon SD, Menon SK, et al. Role of the highly conserved G68 residue in the yeast phosphorelay protein Ypd1: Implications for interactions between histidine phosphotransfer (HPt) and response regulator proteins. *BMC Biochem*. 2019;20(1).
36. Janiak-Spens F, Sparling JM, Gurfinkel M, West AH. Differential stabilities of phosphorylated response regulator domains reflect functional roles of the yeast osmoregulatory SLN1 and SSK1 proteins. *J Bacteriol*. 1999;181:411–417.
37. Xu Q, Nguyen V, West AH. Purification, crystallization, and preliminary X-ray diffraction analysis of the yeast phosphorelay protein YPD1. *Acta Cryst D*. 1999;55:291–293.
38. Janiak-Spens F, West AH. Functional roles of conserved amino acid residues surrounding the phosphorylatable histidine of the yeast phosphorelay protein YPD1. *Mol Microbiol*. 2000;37:136–144.
39. Van Duyne GD, Standaert RF, Karplus PA, Schreiber SL, Clardy J. Atomic structures of the human immunophilin FKBP-12 complexes with FK506 and rapamycin. *J Mol Biol*. 1993;229:105–124.
40. Otwinowski Z, Minor W. Processing of x-ray diffraction data collected in oscillation mode. *Methods Enzymol*. 1997;276:307–326.
41. Winn MD, Ballard CC, Cowtan KD, et al. Overview of the CCP4 suite and current developments. *Acta Cryst D*. 2011;67:235–242.
42. French S, Wilson K. On the treatment of negative intensity observations. *Acta Cryst A*. 1978;34:517–525.
43. Strong M, Sawaya MR, Wang S, Phillips M, Cascio D, Eisenberg D. Toward the structural genomics of complexes: Crystal structure of a PE/PPE protein complex from *Mycobacterium tuberculosis*. *Proc Natl Acad Sci USA*. 2006;103:8060–8065.
44. Pettersen EF, Goddard TD, Huang CC, et al. UCSF Chimera – A visualization system for exploratory research and analysis. *J Comput Chem*. 2004;25:1605–1612.
45. Schrödinger L (2010) The PyMOL Molecular Graphics System, Version 1.3.
46. Søndergaard CR, Olsson MHM, Rostkowski M, Jensen JH. Improved treatment of ligands and coupling effects in empirical calculation and rationalization of pKa values. *J Chem Theory Comput*. 2011;7:2284–2295.
47. Olsson MHM, Søndergaard CR, Rostkowski M, Jensen JH. PROPKA3: Consistent treatment of internal and surface residues in empirical pKa predictions. *J Chem Theory Comput*. 2011;7:525–537.
48. Jurrus E, Engel D, Star K, et al. Improvements to the APBS biomolecular solvation software suite. *Protein Sci*. 2018;27:112–128.
49. Kim B-H, Grishin NV, Pei J. PROMALS3D: A tool for multiple protein sequence and structure alignments. *Nucleic Acids Res*. 2008;36:2295–2300.

50. El-Gebali S, Mistry J, Bateman A, et al. The Pfam protein families database in 2019. *Nucleic Acids Res.* 2019;47:D427–D432.
51. Katoh K, Standley DM. MAFFT multiple sequence alignment software version 7: Improvements in performance and usability. *Mol Biol Evol.* 2013;30:772–780.
52. Clements J, Eddy SR, Finn RD. HMMER web server: Interactive sequence similarity searching. *Nucleic Acids Res.* 2011;39:W29–W37.
53. Humphrey W, Dalke A, Schulten K. VMD—Visual molecular dynamics. *J Mol Graphics.* 1996;14:33–38.
54. Brooks BR, Brooks CL III, MacKerell AD Jr, et al. CHARMM: The biomolecular simulation program. *J Comput Chem.* 2009;30:1545–1615.
55. Phillips JC, Braun R, Wang W, et al. Scalable molecular dynamics with NAMD. *J Comput Chem.* 2005;26:1781–1802.
56. Miller BR, McGee TD, Swails JM, Homeyer N, Gohlke H, Roitberg AE. MMPBSA.py: An efficient program for end-state free energy calculations. *J Chem Theory Comput.* 2012;8:3314–3321.
57. Nguyen H, Roe DR, Simmerling C. Improved generalized born solvent model parameters for protein simulations. *J Chem Theory Comput.* 2013;9:2020–2034.
58. Hawkins GD, Cramer CJ, Truhlar DG. Parametrized models of aqueous free energies of solvation based on pairwise descreening of solute atomic charges from a dielectric medium. *J Phys Chem.* 1996;100:19824–19839.
59. Mongan J, Simmerling C, McCammon JA, Case DA, Onufriev A. Generalized born model with a simple, robust molecular volume correction. *J Chem Theory Comput.* 2007;3:156–169.
60. Onufriev A, Bashford D, Case DA. Exploring protein native states and large-scale conformational changes with a modified generalized born model. *Proteins.* 2004;55:383–394.
61. Gohlke H, Kiel C, Case DA. Insights into protein–protein binding by binding free energy calculation and free energy decomposition for the Ras–Raf and Ras–RalGDS complexes. *J Mol Biol.* 2003;330:891–913.

SUPPORTING INFORMATION

Additional supporting information may be found online in the Supporting Information section at the end of this article.

How to cite this article: Branscum KM, Menon SK, Foster CA, West AH. Insights revealed by the co-crystal structure of the *Saccharomyces cerevisiae* histidine phosphotransfer protein Ypd1 and the receiver domain of its downstream response regulator Ssk1. *Protein Science.* 2019;28:2099–2111. <https://doi.org/10.1002/pro.3755>